Single-Crystal Spectroscopic Studies of $Fe(SR)_4^{2-}$ (R = 2-(Ph)C_6H_4): Electronic Structure of the Ferrous Site in Rubredoxin

Matthew S. Gebhard,[§] Stephen A. Koch,[†] Michelle Millar,[†] Frank J. Devlin,[‡] Philip J. Stephens,[‡] and Edward I. Solomon*[,§]

Contribution from the Department of Chemistry, Stanford University, Stanford, California 94305, Department of Chemistry, SUNY Stony Brook, Stony Brook, New York 11794, and Department of Chemistry, University of Southern California, Los Angeles, California 90089.
Received July 16, 1990

Abstract: Low-temperature single-crystal magnetic circular dichroism (MCD) and polarized absorption studies were performed on an axial ferrous rubredoxin structural model complex, $[Et_4N]_2[Fe(SR)_4]$ (R = 2-(Ph)C_6H_4). This complex was found to have a $d_{x^2-y^2}$ ground state with the d_{z^2} orbital at 1400 cm^{-1}. A ligand field analysis of the observed and assigned $^5E \rightarrow {}^5T_2$ and $^5E \rightarrow {}^3\Gamma$ transitions gives $Dq = -350$ cm^{-1}, $C = 2800$ cm^{-1}, and $B = 620$ cm^{-1}. In contrast to ferric thiolate complexes which exhibit much larger reductions, the 70% reduction in ferrous electron repulsion parameters from the free ion values is accounted for based on standard spin restricted ligand field theory. This indicates that the inverted bonding description found for ferric complexes is not present in the ferrous complexes. Thus a large electronic relaxation takes place upon reduction which should affect redox properties of iron thiolate complexes. A calculation of the ground-state zero-field splitting based on spin-orbit coupling to the $^5T_2$ and $^3\Gamma$ ligand field excited states gives $D_{calc} = -8.7$ cm^{-1} which is in excellent agreement with $D_{exp} = -8.7 \pm 0.7$ cm^{-1} as determined from the MCD temperature dependence. The splitting of the ferrous 3d orbitals is found to depend on the interactions with the S-Feσ bonding orbital as determined by the αC orientation. This effect accounts for the ground-state differences between the model complex and ferrous rubredoxin and reveals a strong dependence of the ground state on the αC orientation.

Introduction

Iron-sulfur proteins are a broad class of electron-transfer proteins[1] distinguished by the presence of one, two, three, and four iron-sulfur clusters. The iron in these systems is approximately tetrahedral with all cysteinyl coordination for the one iron center and mixed cysteinyl and bridging sulfide ligation in the clusters. Rubredoxin[1] is the prototype single iron sulfur center, containing an approximately D_{2d} distorted $[Fe(S\text{-}cys)_4]^{-/2-}$ complex (Figure 1). The X-ray crystal structure[2] of ferric *Clostridium pasteurianum* (*Cp*) rubredoxin has been solved to 1.2-Å resolution. The crystal structure of ferrous *Cp* rubredoxin has only been solved to 4-Å resolution; however, it is known from EXAFS studies[3] that the Fe-S bond lengths increase only slightly (<0.06 Å) upon reduction of the ferric protein. Rubredoxin has a reduction potential[1] of -0.06 V relative to a standard hydrogen electrode and a fast electron transfer self exchange rate[4] of roughly 10^9/s.

An understanding of the redox mechanism of rubredoxin and iron-sulfur proteins is of great interest as it applies to the general question of biological electron-transfer processes. While there have been many interesting studies of rubredoxin,[5] the lack of detailed spectroscopic data on both oxidation states has left many unanswered questions concerning the intrinsic electronic structure characteristics of these iron tetrathiolate complexes and their relationship to the redox properties of these proteins. Therefore we have undertaken a series of studies aimed at understanding the relationship between the redox properties and the geometric and electronic structure of the iron tetrathiolate complexes.

In our previous work[6] single-crystal polarized absorption, MCD, and EPR were employed to define the electronic structure of an S_4 ferric rubredoxin model complex ($[Fe(SR)_4][N(C_2H_5)_4]$, where R = 2,3,5,6-$(CH_3)_4C_6H$). This study revealed an extreme reduction in the energies of the spin-forbidden $^6A_1 \rightarrow {}^4\Gamma$ d $\rightarrow$ d transitions. The observation of these low-energy transitions has required an alternative description[7] of bonding relative to the standard spin restricted ligand field theory. Bonding interactions in this ferric complex are dominated by large spin-polarization effects, producing the inverted bonding pattern given in Figure 2 which places the unpaired spin-up electrons in mostly ligand centered valence orbitals, while the empty spin-down orbitals are mostly metal centered. A second conclusion of this study was the strong influence of the off-axis thiolate S-Feσ bonding orbital on the Fe(III) d orbital splitting pattern, while the S-Feπ bonding

[§] Stanford University.
[†] SUNY Stony Brook.
[‡] University of Southern California.

(1) (a) *Iron Sulfur Proteins*; Lovenberg, W., Ed.; Academic Press: New York, 1973; Vols. I and II. (b) *Iron Sulfur Proteins*; Lovenberg, W., Ed.; Academic Press: New York, 1977; Vol. III. (c) *Metal Ions In Biology* Vol. IV. *Iron Sulfur Proteins*; Spiro, T. G., Ed.; Wiley-Interscience: New York, 1982.

(2) (a) Watenpaugh, K. D.; Sieker, L. C.; Jensen, L. H. *J. Mol. Biol.* **1979**, *131*, 509. (b) Watenpaugh, K. D.; Sieker, L. C.; Jensen, L. H. *J Mol. Biol.* **1980**, *138*, 615.

(3) (a) Shulman, R. G.; Eisenberger, P.; Teo, B. K.; Kincaid, B. M.; Brown, G. S. *J. Mol. Biol.* **1978**, *124*, 305. (b) Shulman, R. G.; Eisenberger, P.; Blumberg, W. E.; Stombaugh, N. A. *Proc. Natl. Acad. Sci. U.S.A.* **1975**, *72*, 4003.

(4) Jacks, C. A.; Bennett, L. E.; Raymond, W. N.; Lovenberg, W. *Proc. Natl. Acad. Sci. U.S.A.* **1974**, *71*, 1118.

(5) (a) Muraoka, T.; Nozawa, T.; Hatano, M. *Inorg. Chim. Acta* **1986**, *124*, 49. (b) Rivoal, J. C.; Briat, B.; Cammack, R.; Hall, D. O.; Rao, K. K.; Douglass, I. N.; Thomson, A. J. *Biochim. Biophys. Acta* **1977**, *493*, 122. (c) Eaton, W. A.; Palmer, G.; Fee, J. A.; Kimura, T.; Lovenberg, W. *Proc. Natl. Acad. Sci. U.S.A.* **1971**, *68*, 3015. (d) Long, T. V.; Loehr, T. M. *J. Am. Chem. Soc.* **1970**, *92*, 6384. (e) Long, T. V.; Loehr, T. M.; Allkins, J. R.; Lovenberg, W. *J. Am. Chem. Soc.* **1971**, *93*, 1809. (f) Yachandra, V. K.; Hare, J.; Moura, I.; Spiro, T. G. *J. Am. Chem. Soc.* **1983**, *105*, 6455. (g) Czernuszewicz, R. S.; LeGall, J.; Moura, I.; Spiro, T. G. *Inorg. Chem.* **1986**, *25*, 696. (h) Peisach, J.; Blumberg, W. E.; Lode, E. T.; Coon, M. J. *J. Biol. Chem.* **1971**, *246*, 5877. (i) Phillips, W. D.; Poe, M.; Weihler, J. F.; McDonald, C. C.; Lovenberg, W. *Nature (London)* **1970**, *227*, 574. (j) Thomson, C. L.; Jackson, P. J.; Johnson, C. E. *Biochem. J.* **1972**, *129*, 1063. (k) Lane, R. W.; Ibers, J. A.; Frankel, R. B.; Papaefthymiou, G. C.; Holm, R. H. *J. Am. Chem. Soc.* **1977**, *99*, 84. (l) Deaton, J. C.; Gebhard, M. G.; Koch, S. A.; Miller, M.; Solomon, E. I. *J. Am. Chem. Soc.* **1988**, *110*, 6241. (m) Bennett, D. E.; Johnson, M. K. *Biochim. Biophys. Acta* **1987**, *911*, 71. (n) Ueyama, N.; Sugawara, T.; Tatsumi, K.; Nakamura, A. *Inorg. Chem.* **1987**, *26*, 1978. (o) Bair, R. A.; Goddard, W. A., III *J. Am. Chem. Soc.* **1978**, *100*, 5669. (p) Noodleman, L.; Norman, J. G., Jr.; Osborne, J. H.; Aizman, A.; Case, D. A. *J. Am. Chem. Soc.* **1985**, *107*, 3418. (q) Norman, J. G., Jr.; Jackels, S. C. *J. Am. Chem. Soc.* **1975**, *97*, 3833. (r) Bertrand, P.; Gayda, J. P. *Biochim. Biophys. Acta* **1988**, *954*, 347.

(6) Gebhard, M. S.; Deaton, J. C.; Koch, S. A.; Millar, M.; Solomon, E. I. *J. Am. Chem. Soc.* **1990**, *112*, 2217.

(7) (a) Butcher, K. D.; Gebhard, M. S.; Solomon, E. I. *Inorg. Chem.* **1990**, *29*, 2067. (b) Butcher, K. D.; Didziulis, S. V.; Briat, B.; Solomon, E. I. *J. Am. Chem. Soc.* **1990**, *112*, 2231.

0002-7863/91/1513-1640$02.50/0

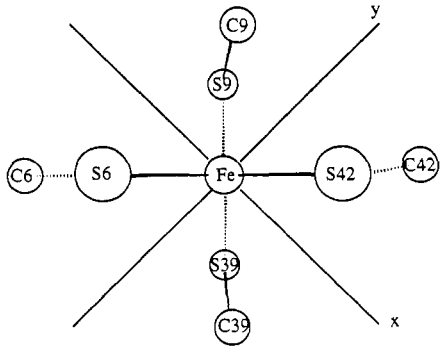

Figure 1. $Fe(SR)_4$ center of ferric *Cp* rubredoxin viewed down the pseudo-C_2 axis. Adapted from ref 2.

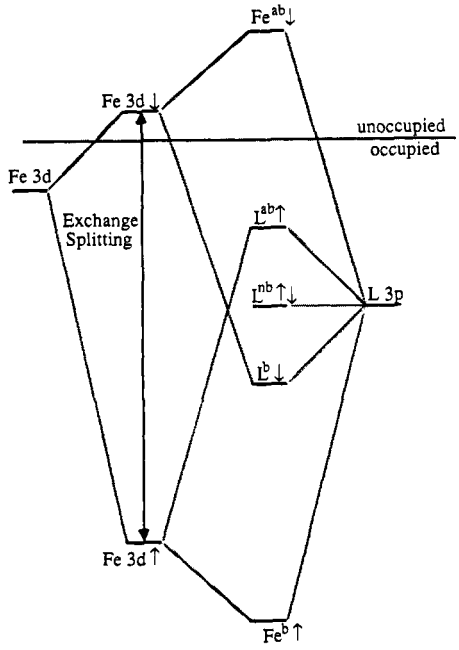

Figure 2. Spin-unrestricted bonding scheme for high-spin ferric complexes.

interaction was found to be insignificant. It was also found that the ground-state zero-field splitting resulted from the effects of anisotropic covalency on the Fe(III) d orbitals. This study yielded important insight into the electronic structure of ferric tetrathiolate complexes, and its influence on electron-transfer processes. However, a thorough understanding of the electronic structure of ferrous tetrathiolate and thus the changes which occur upon reduction is essential for an understanding of the electron-transfer properties of these systems.

High-spin tetrahedral ferrous complexes are characterized[8] by having a ^5E ground state with a low-lying $^5T_2$ excited state at $10Dq$ (3000–5000 cm^{-1}) above the ground state (Figure 3). Typically the orbital components ($^5E\theta(d_{z^2})$ and $^5E\epsilon(d_{x^2-y^2})$) of the ^5E are split by an axial low-symmetry component (S_4 in Figure 3) of the ligand field producing either a pure d_{z^2} or $d_{x^2-y^2}$ ground state. The axial distortion will also split the $^5T_2$ into the $^5T_2(\pm1)(d_{xz,yz})$ and $^5T_2(0)(d_{xy})$ orbital components. Second-order spin–orbit interactions with the ligand-field excited states will produce an additional zero-field splitting of the M_s ground-state components. In axial symmetry this splitting (shown on the right side of Figure 3 for negative *D*) is described by the spin Hamiltonian parameter, *D*, which is typically about 10 cm^{-1}. In addition to the spin-allowed transitions there are a large number of spin-forbidden $^5E \rightarrow {}^3\Gamma$ transitions (Figure 3) which occur in the visible region with $\epsilon \approx 5\ M^{-1}\ cm^{-1}$. These transitions are important as they give information about electron repulsion parameters, and the extent of spin polarization in these complexes. The charge-transfer transitions for ferrous complexes typically occur in the UV region and are seldom observed as they are often obscured by more intense ligand-centered transitions.

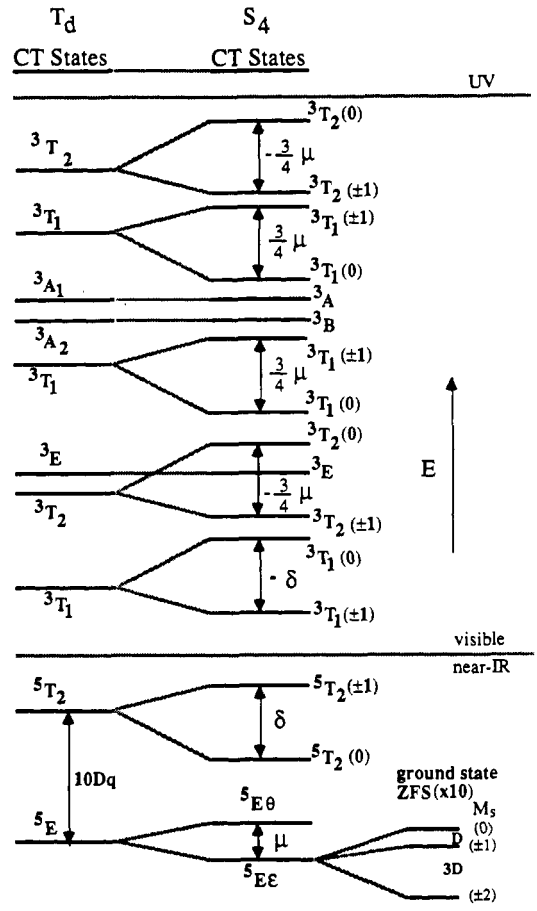

Figure 3. High-spin ferrous energy level diagram showing relative energies of ground-state ZFS, along with quintet, triplet, and charge-transfer excited states.

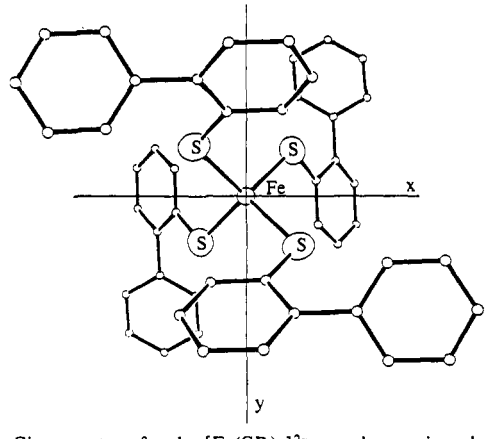

Figure 4. Site structure for the $[Fe(SR)_4]^{2-}$ complex as viewed down the molecular S_4 (*z*) axis.

Reduced rebredoxin has been investigated by near-IR CD[9] and Mossbauer[10] spectroscopies. From these studies it is known that a component of the $^5E \rightarrow {}^5T_2$ d → d transition occurs at roughly 6000 cm^{-1}, which is rather high for a T_d ferrous complex. The ground state is d_{z^2} with the $d_{x^2-y^2}$ state at least 1000 cm^{-1} higher in energy. Unfortunately the $^5E \rightarrow {}^3\Gamma$ transitions have not been

(8) Lever, A. B. P. *Inorganic Electronic Spectroscopy*, 2nd ed.; Elsevier Science Publishers: Amsterdam, 1984.

(9) Eaton, W. A.; Lovenberg, W. *J. Am. Chem. Soc.* **1970**, *92*, 7195.
(10) Rao, K. K.; Evans, M. C. W.; Cammack, R.; Hall, D. O.; Thomson, C. L.; Jackson, P. J.; Johnson, C. E. *J. Biochem.* **1972**, *129*, 1063.

observed due to their weak intensity. While the spectroscopic data on the protein are significant it provides limited insight into the ferrous electronic structure. Therefore a detailed electronic structure study of a ferrous tetrathiolate model complex has been undertaken.

The geometry[11] of the model complex that was chosen is similar (Figure 4) to the geometry of rubredoxin in that both have an approximately T_d FeS_4 core; however, one major difference does exist. In Cp rubredoxin the dihedral angle between the S–Fe–S plane and the Fe–S–αC is close to 180° with the αC pointed down toward the x,y plane of the molecule (Figure 1). In the model complex the dihedral angle is about 47° (Figure 4). The model complex has strict S_4 site symmetry and crystallizes in an axial space group ($I\bar{4}C2$) which is rare for a ferrous complex. The high symmetry is crucial for detailed single-crystal studies. This ferrous model complex is also very similar to the previously studied ferric model complex, allowing rigorous comparisons.

In the present study single-crystal polarized absorption and MCD spectra of the spin-allowed and spin-forbidden d → d transitions of $[N(C_2H_5)_4]_2[Fe(SR)_4]$ (R = 2-(Ph)C_6H_4) are reported, as is the ground-state zero-field splitting as determined from the temperature dependence of the MCD signal. These data are analyzed by using selection rules based on vector coupling coefficients which allow a rigorous assignment of the spectrum. A spectroscopic comparison between the oxidized and reduced model complex is presented along with a comparison to similar data on ferric and ferrous chloride complexes. A comparison is made between reduced rubredoxin and the model complex. Also an evaluation of the accepted model for ferrous ^5E zero-field splittings is presented.

Experimental Section

$[Et_4N]_2[Fe(SR)_4]$ (R = 2-(Ph)C_6H_4) was prepared by mixing ethanol solutions of LiSR and anhydrous $FeCl_2$ with a 5:1 mol ratio. The solution was stirred for approximately 10 min, and the complex was precipitated as the Et_4N^+ salt. The reaction was run under N_2 with deoxygenated solvents. Single crystals of $[Et_4N]_2[Fe(SR)_4]$ were grown by dissolving the complex in hot dry deoxygenated CH_3CN. The solution was filtered and allowed to cool slowly over several days. The compound crystallizes[11] in the $I\bar{4}C2$ space group growing as pale green plates (2–3 mm on edge) with the (001) face being the most prominent. The iron atom occupies a site of rigorous S_4 site symmetry, with the molecular S_4 axis (z axis) coinciding with the crystal c axis. The FeS_4 core (Figure 4) is slightly distorted from tetrahedral symmetry with a compression along the S_4 axis causing the S–Fe–S angles bisected by the S_4 axis to open to 113.4°. The other four angles are 107.5°. The Fe–S bond length is 2.338 ± 0.002 Å. The zinc(II) analogue is isomorphous to the Fe(II) salt and is used as a host lattice for experiments requiring dilute concentrations of the ferrous complex. The zinc salt was prepared with $ZnCl_2$ by the above procedure. Doped crystals were grown as with the pure crystals after mixing the desired amounts of the Zn and Fe compounds.

Solution spectra were carried out in deoxygenated CH_3CN. The compound crystallizes with CH_3CN in the lattice and thus had a tendency to dry out over several days causing the faces to become cloudy. Therefore in the single-crystal optical experiments, the (001) or (010) face was mounted flush against an infrasil quartz window and covered with poly(vinyl acetate) (PVA) dissolved in CH_3CN. This kept the faces of the crystals from clouding and allowed them to be polished after the CH_3CN had evaporated. The PVA was useful because it is fairly transparent[12] in the spectral regions of interest. After being polished to the desired thickness with 9 μm grit lapping film or a homemade polishing apparatus the crystals were masked off around the edges with black electrical tape. The polarized absorption spectrum was recorded with the **E** vector polarized parallel or perpendicular to the c axis. Single-crystal MCD spectra were recorded on crystals which were cut and polished on the (001) face and prepared in the same manner as for the optical experiments. In this orientation light is propagated down the crystal c axis, such that the **E** vector only projects on the molecular x,y axis. Depolarization of the light by the MCD samples was monitored by the effect the sample had on the CD signal of nickel (+)-tartrate placed before and after the sample. Samples which decreased the CD signal by less than 5% were considered suitable.

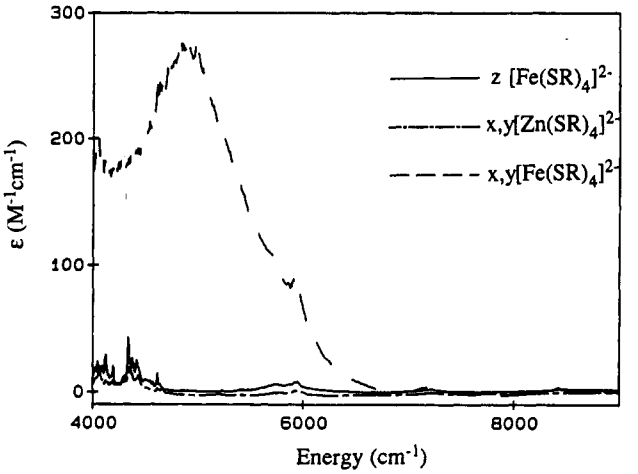

Figure 5. Polarized absorption spectra at 7 K for a 100 μm thick $[N(Et)_4]_2[Zn(Fe)\text{-}(SR)_4]$ ([Fe] = 30%) crystal taken on the (010) face and a 225 μm thick $[N(Et)_4]_2[Zn(SR)_4]$ crystal taken on the (001) face.

Polarized absorption spectra were measured on a McPherson RS-10 double beam spectrophotometer described previously,[13] but with upgraded electronics. A pair of Glan-Taylor polarizers matched from 200 nm to 2.5 μm were used in the sample and reference beams. Three gratings blazed at 3000 Å, 7500 Å, and 1.25 μm were used to cover the different spectral regions. An extended S-20 photomultiplier tube covered the region from 5000 to 8500 Å and a Joule-Thompson cooled PbS detector was used from 8000 Å to 2.5 μm. The latter detector required use of a chopped (560 Hz) light source and a lock-in amplifier. A 1.1 μM cutoff filter manufactured by Optical Coatings Laboratories Incorporated (p/n 101047-8) was used to eliminate the contributions from second-order light in the near-IR region. The light source was a tungsten–halogen lamp. A Janis Super-Vari Temp dewar was used for the liquid He temperature absorption experiments. MCD spectra were recorded on a JASCO J-500C CD spectropolarimeter configured[14] with an Oxford SM4 superconducting magnet and focussing optics. The near-IR MCD spectrum was recorded on a specially designed instrument as described previously.[15]

Results

(A) Near-IR Region. (i) Polarized Absorption. The 7 K polarized absorption spectrum on a $[Et_4N]_2[Zn(Fe)\text{-}(SR)_4]$ ([Fe^{II}] = 30%) single crystal from 4000 to 10000 cm^{-1} is presented in Figure 5. Comparison with the x,y absorption spectrum of the pure Zn compound (Figure 5) reveals that the 4600 cm^{-1} x,y polarized absorption feature (ϵ = 270 M^{-1} cm^{-1}) is truly an electronic absorption band as opposed to a vibrational overtone band due to either the PVA or the compound. This is the only detectable electronic transition between 12000 and 4000 cm^{-1}.

(ii) Magnetic Circular Dichroism. The 2 K and 3 kG near-IR MCD spectrum on a 30% Fe(II) doped $[Et_4N]_2[Zn(Fe)\text{-}(SR)_4]$ crystal is shown in Figure 6. The x,y polarized absorption spectrum is also included, since for an oriented uniaxial single crystal it is necessary but not sufficient for a band to have x,y polarized intensity in order to have non-zero MCD intensity. The MCD signal exhibits C term temperature dependence and from a comparison to the polarized absorption it appears to be a positive pseudo-A term arising from the 4600 cm^{-1} electronic absorption band.

(B) Visible Region. (i) Polarized Absorption. The 7 K polarized absorption spectrum between 12000 and 20000 cm^{-1} on a $[Et_4N]_2[Fe(SR)_4]$ single crystal is presented in Figure 7. The spectrum has a set of weak (ϵ < 10 M^{-1} cm^{-1}) transitions, which based on their intensities are clearly the spin-forbidden $^3\Gamma$ states

(11) Millar, M.; Koch, S. A. To be submitted for publication.

(12) PVA does have overtone bands in the near-IR region, but from a comparison to the spectrum of a 300-μm sample of PVA it was determined that its contribution to the spectrum was negligible. This can also be seen from the spectrum of the $Zn(SR)_4^{2-}$ analogue which was recorded with similar conditions and should have a similar contribution from the PVA.

(13) Wilson, R. B.; Solomon, E. I. *Inorg. Chem.* **1978**, *17*, 1729.

(14) Allendorf, M. D.; Spira, D. J.; Solomon, E. I. *Proc. Natl. Acad. Sci. U.S.A.* **1985**, *82*, 3063.

(15) Osborne, G. A.; Cheng, J. C.; Stephens, P. J. *Rev. Sci. Instrum.* **1973**, *44*, 10.

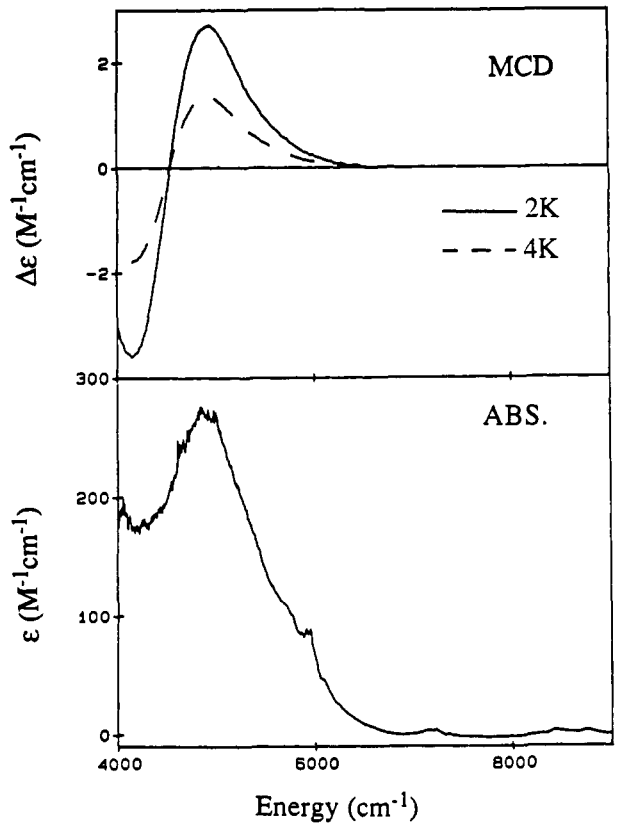

Figure 6. 3 kG single-crystal MCD spectrum at 4 K (dashed) and 2 K (solid) of a 70 μm thick $[N(Et)_4]_2[Zn(Fe)\text{-}(SR)_4]$ ([Fe] = 30%) crystal taken on the (001) face.

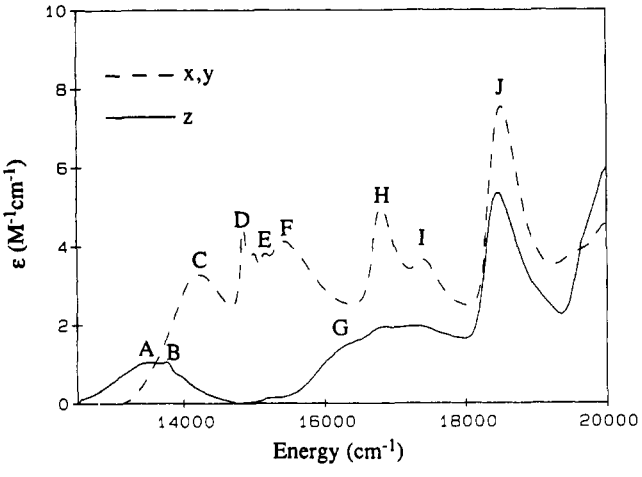

Figure 7. Polarized absorption spectrum at 7 K for a 1.5 mm thick $[N(Et)_4]_2[Fe(SR)_4]$ crystal taken on the (010) face.

of the ferrous center. The ten bands are labeled A–J. Bands A, B, and G are purely z polarized and bands C, D, E, and F are purely x,y polarized. Bands I and J exhibit mixed polarizations. Table I lists the energies and polarization characteristics of these bands.

(ii) Magnetic Circular Dichroism. The 7 K and 20 kG MCD spectrum from 12000 to 20000 cm^{-1} of a $[Et_4N]_2[Fe(SR)_4]$ single crystal is presented in Figure 8 along with the corresponding x,y polarized absorption spectrum. All of the MCD signals exhibited temperature-dependent C term behavior. Bands C, F, and I give rise to positive C terms, while bands D, E, H, and J give rise to negative C terms. This information is listed in Table I. It is also observed that between 25000 and 40000 cm^{-1} there are no MCD active transitions (Figure 9).

The saturation behavior of the MCD signal for a $[Et_4N]_2[Fe(SR)_4]$ single crystal at 542 nm and 2 K (Figure 8, band J)

Table I

band	energy, cm^{-1}	polarization	MCD	assign	calcd energy, cm^{-1}
A	13550	z	0	$^3T_1^{(a)}(\pm1)$	12070
B	13900	z	0	$^3T_2^{(a)}(\pm1)$	14000
C	14200	x, y	positive	$^3T_1^{(a)}(0)$	12770
D	14850	x, y	negative	$^3E^{(a)}$	14850
E	15000	x, y	negative	$^3T_2^{(a)}(0)$	15050
F	15375	x, y	positive	$^3T_1^{(b)}(0)$	15500
G	16440	z	0	$^3T_1^{(b)}(\pm1)$	16550
H	16800	x, y	negative	$^3A_2$	16700
I	17400	x, y, z	positive	$^3T_1^{(c)}$	17100
J	18500	x, y, z	negative	$^3T_2^{(b)}$	19000

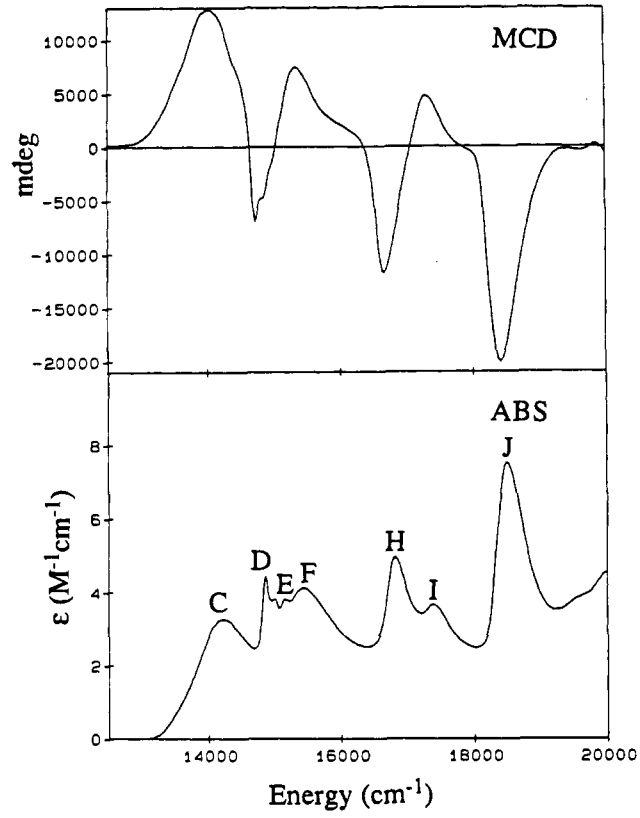

Figure 8. (Top) Single-crystal MCD spectrum at 50 kG and 4.2 K for a 0.5 mm thick $[N(Et)_4]_2[Fe(SR)_4]$ crystal taken on the (001) face. (Bottom) x,y polarized absorption spectrum at 7 K for a 100 μm thick $[N(Et)_4]_2[Zn(Fe)\text{-}(SR)_4]$ crystal taken on the (001) face.

is presented in Figure 10. From a fit of the intensity to eq 1, $g_z = 8.24 \pm 0.06$. These data indicate a negative zero-field

$$I(\beta H/2kT) = I_0 \tanh (g_z\beta H/2kT) \quad (1)$$

splitting (Figure 3) as the $M_s = \pm2$ ($g_z \approx 8$) is the lowest spin state. The same g_z values were obtained to within experimental error at 2 and 4 K indicating no measurable population of the $M_s = \pm1$ state is occurring up to 4 K. All of the other MCD bands (A–I) in this region show identical saturation behavior, meaning these transitions clearly originate from the Fe(II) complex.

Figure 11 shows the temperature dependence of the 542-nm MCD feature. The integrated intensity was measured at low values of $g\beta H/2kT$ ($g\beta H/2kT < 0.2$) to avoid complications due to saturation of the MCD signal. The intensity was normalized to the same magnetic field and is plotted versus $1/T$. The intensity is not a linear function of $1/T$ indicating population of a low-lying excited sublevel of the ground-state spin manifold. The axial zero-field splitting of the ^5E state will cause $M_s = \pm1$ and 0 spin states to lie 3 and 4 D above the $M_s = \pm2$ ground state (Figure 11 inset). Only the $M_s = \pm2$ and ±1 states will have an MCD contribution; however, the $M_s = 0$ state will affect the MCD

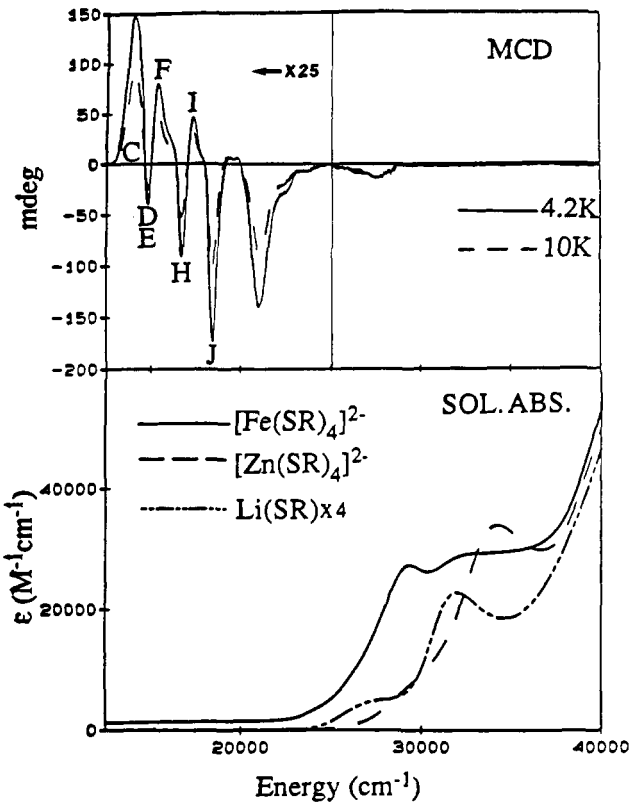

Figure 9. (Top) Single-crystal MCD spectrum at 50 kG for a 100 μm thick $[N(Et)_4]_2[Zn(Fe)\text{-}(SR)_4]$ ([Fe = 0.2%) crystal taken on the (001) face. The MCD features below 25 000 cm^{-1} have been multiplied by 25. (Bottom) Room temperature solution absorption spectra for $[Fe(SR)_4]^{2-}$, $[Zn(SR)_4]^{2-}$, and LiSR. The LiSR spectra has been multiplied by four.

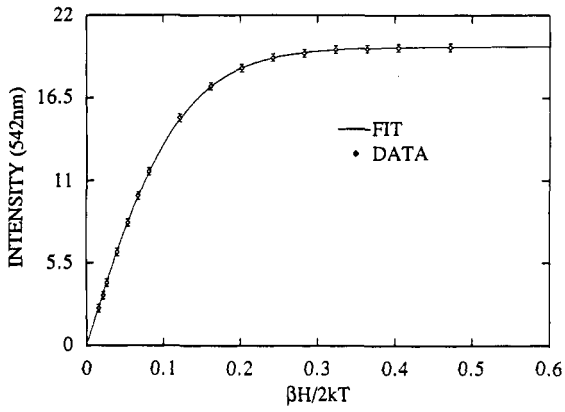

Figure 10. MCD saturation data at 4.2 K and 542 nm (band J) for a 200 μm thick $[N(Et)_4]_2[Fe(SR)_4]$ crystal taken on the (001) face.

through its effect on the population of the $M_s = \pm1$ and ±2 levels. A fit to a three-state model, eq 2, gives $D = -8.7 \pm 0.7$ cm^{-1}, with

$$I(T) = \frac{(2I_{\pm2} + 2I_{\pm1}e^{(-3D/kT)})}{(2 + 2e^{(-3D/kT)} + e^{(-4D/kT)})} \quad (2)$$

$I_{\pm2} = 2300$ and $I_{\pm1} = 1600$, where $I_{\pm1}$ and $I_{\pm2}$ are the MCD intensities from the $M_s = \pm1$ and ±2 spin states, respectively.

(iii) Solution Absorption. The room temperature absorption spectra in the 12500–40000-cm^{-1} region for the $[Et_4N]_2[Zn(SR)_4]$, $[Et_4N]_2[Fe(SR)_4]$, and LiSR compounds are presented in Figure 9. A series of very intense transitions ($\epsilon \approx 30\,000$ M^{-1} cm^{-1}) are observed in all three compounds. These are clearly ligand-centered transitions in the $[Et_4N]_2[Zn(SR)_4]$ and LiSR compounds. On the basis of the lack of MCD C term activity (Figure 9) these transitions must also be ligand centered in the $[Et_4N]_2[Fe(SR)_4]$ compound. In earlier studies of reduced rubredoxin a MCD signal is observed[1] at 28 500 cm^{-1} ($\epsilon \approx 5000$ M^{-1} cm^{-1}) which was

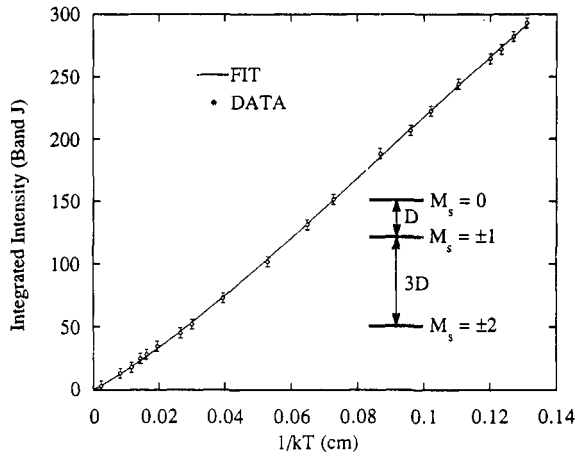

Figure 11. Temperature dependence of the integrated MCD intensity (bank J) for a 200 μm thick $[N(Et)_4]_2[Fe(SR)_4]$ crystal taken on the (001) face.

tentatively assigned as a Fe(II) to S CT transition. It is likely that this transition exists in the model complex but is obscured by the intense ligand-centered transitions in this region.

Analysis

(A) Selection Rules for Polarized Absorption. It is evident from the highly polarized nature of the ligand field transitions in the $Fe(SR)_4^{2-}$ complex (Figures 5 and 7) that the effective site symmetry is axial even though the FeS_4 core of the molecule is only slightly distorted from the tetrahedral structure. Thus the spectral analysis should be performed with use of the S_4 axial subgroup; however, an equivalent treatment can be employed which utilizes the T_d wave functions with a tetragonal (D_{2d}) distortion, and this procedure is followed below for the spin-forbidden states. This treatment is valid because of the subgroup relationship between T_d, D_{2d}, and S_4 and has the advantage that the S_4 states can be more easily related to the parent T_d states, thus providing more information about the transition. Selection rules derived in this manor are strictly valid in D_{2d} symmetry and will be valid in S_4 symmetry as long as mixing between states which transform as A_1 and A_2 or B_1 and B_2 in D_{2d} symmetry is negligible in the lower symmetry S_4 subgroup. The S_4 distortion will split the T_d orbital doublet (^{2s+1}E) states into $^{2s+1}E\epsilon$ and $^{2s+1}E\theta$ component states while the orbital triplet ($^{2s+1}T_2$ and $^{2s+1}T_1$) states will be split into $^{2s+1}T(\pm1)$ and $^{2s+1}T(0)$ component states. In addition states which transform as A_2 or A_1 in T_d will transform as B or A respectively in S_4 symmetry.

In tetrahedral symmetry a high-spin Fe(II) complex will have a ^5E ground state with a $^5T_2$ excited state at $10Dq(T_d)$ (3000–5000 cm^{-1}) above the ground state (Figure 3). As the complex is distorted to S_4 symmetry the ^5E ground state will split, yielding either a $^5E\theta(d_{z^2})$ or a $^5E\epsilon(d_{x^2-y^2})$ ground state. Also the $^5T_2$ excited state will split into $^5T_2(\pm1)(d_{xz,yz})$ and $^5T_2(0)(d_{xy})$ states. If the $^5E\theta(d_{z^2})$ state is lowest then two transitions from the $^5E\theta(d_{z^2})$ ground state to the two components of the $^5T_2$ excited state are electric dipole allowed ($^5E\theta \rightarrow {}^5T_2(0)$ in z polarization, $^5E\theta \rightarrow {}^5T_2(\pm1)$) in x,y polarization). If the $^5E\epsilon(d_{x^2-y^2})$ is lowest then only the $^5E\epsilon \rightarrow {}^5T_2(\pm1)$ transition is electric dipole allowed in x,y polarization. If both the $^5E\theta(d_{z^2})$ and $^5E\epsilon(d_{x^2-y^2})$ states are populated then all three transitions will be observed, and the splitting between the two x,y polarized states gives the splitting between the $d_{x^2-y^2}$ and d_{z^2} orbitals. Therefore the polarized absorption can be used to define the orbital character of the Fe(II) ground state. These selection rules are summarized in Table II (columns 2 and 3) and were derived by using the S_4 point group (in S_4 symmetry $E\epsilon$, $E\theta$, $T_2(0)$, $T_2(\pm1)$, m_z, and $m_{x,y}$ transform as B, A, B, E, B, and E, respectively).

In addition to these low-energy spin-allowed transitions, a set of $^5E \rightarrow {}^3\Gamma$ spin-forbidden transitions is expected in the visible region with $\epsilon \approx 1$–10 M^{-1} cm^{-1} (Figure 3). These transitions gain intensity through spin–orbit coupling with electric dipole allowed

Table II

$^5T_2h'$	pol. $^5E\epsilon^a$	pol. $^5E\theta^b$	MCD $^5E\epsilon^a$	MCD $^5E\theta^b$	obs (pol.)	calcd, cm^{-1}
$^5T_2(\pm1)$	x, y	x, y	positive pseudo-A term	negative pseudo-A term	4600 (x, y)	4480
$^5T_2(0)$		z	negative C term	positive C term		3780

[a] Assumes a $^5E\epsilon$ ground state. [b] Assumes a $^5E\theta$ ground state.

Table III

$^3\Gamma h'$	pol. $^5E\epsilon(\pm2)^a$	pol. $^5E\theta(\pm2)^b$	MCD $^5E\epsilon(\pm2)^a$	MCD $^5E\theta(\pm2)^b$
$^3T_1(0)$	x, y	x, y	positive	negative
$^3T_1(\pm1)$	z	z	0	0
$^3T_2(0)$	x, y	x, y	negative	positive
$^3T_2(\pm1)$	z	z	0	0
$^3E(\epsilon,\theta)$	x, y	x, y	negative	negative
$^3A_2$	x, y	x, y	negative	positive
$^3A_1$	x, y	x, y	positive	negative

[a] Assumes a $^5E\epsilon$ ground state with only the $M_s = \pm2$ populated. [b] Assumes a $^5E\theta$ ground state with only the $M_s = \pm2$ populated.

transitions.[16] This occurs through spin–orbit coupling of $^5T_2$ character into the $^3\Gamma$ excited states and spin–orbit coupling of $^3T_1$ and $^3T_2$ character into the ^5E ground state. These mechanisms are described by eq 3, where M_s and M_s' represent the spin

$$\langle {}^5EhM_s|m_q|{}^3\Gamma h'M_s'\rangle = \frac{\langle {}^5EhM_s|m_q|{}^5T_2h''M_s\rangle\langle {}^5T_2h''M_s|H_{so}|{}^3\Gamma h'M_s'\rangle}{E(^5T_2) - E(^3\Gamma)} + \frac{\langle {}^5EhM_s|H_{so}|{}^3T_2h''M_s'\rangle\langle {}^3T_2h''M_s'|m_q|{}^3\Gamma h'M_s'\rangle}{E(^3T_2) - E(^5E)} + \frac{\langle {}^5EhM_s|H_{so}|{}^3T_1h''M_s'\rangle\langle {}^3T_1h''M_s'|m_q|{}^3\Gamma h'M_s'\rangle}{E(^3T_1) - E(^5E)} \quad (3)$$

components; h, h', and h'' are the orbital components; m_q is the electric dipole operator ($q = x, y, z$ or $0, +1, -1$); and H_{so} is the spin orbit coupling operator. Except for differences in phase relationships the three contributions yield the same selection rules for all $^3\Gamma$ excited states, and these selection rules are given in Table III, using the T_d parent notation.

Because these $^5E \rightarrow {}^3\Gamma$ transitions gain intensity through spin–orbit coupling, the transition moments depend on the M_s sublevel of the ground state. This leads to an interesting effect when only the $M_s = \pm2$ spin component is populated. On the basis of the above intensity mechanism the $^5E(\epsilon$ or $\theta, M_s=\pm2) \rightarrow {}^3T_{1or2}(\pm1)$ transitions are not allowed in x,y polarization, whereas the transitions from the $M_s = \pm1$ and 0 sublevels will be allowed in x,y polarization. In addition the $^5E(\epsilon, M_s=\pm2) \rightarrow {}^3A_1$, $^5E(\theta, M_s=\pm2) \rightarrow {}^3A_2$, $^5E(\epsilon, M_s=\pm2) \rightarrow {}^3E\theta$, and $^5E(\theta, M_s=\pm2) \rightarrow {}^3E\epsilon$ transitions are not allowed in z polarization, whereas the transitions from the $M_s = \pm1$ and 0 sublevels will be allowed in z polarization. This effect will be significant when D is negative and large ($|D| > 5\ cm^{-1}$) as selective population of the $M_s = \pm2$ sublevels can be achieved at low temperature ($T < 10$ K). Because only the $M_s = \pm2$ state is populated in the low-temperature MCD and polarized absorption spectra (Figures 5–8) only the low-temperature selection rules are included in Table III.

(B) Selection Rules for Single-Crystal Magnetic Circular Dichroism. For a paramagnetic molecule oriented such that the magnetic field is parallel to the molecular z axis, the dominant contribution[17] to the MCD signal is described by eq 4. γ depends

$$\left(\frac{\Delta A}{E}\right) = \frac{\gamma C_0 \mu_B B f(E)}{kT} \quad (4)$$

on constants such as the dielectric constant and refractive index,

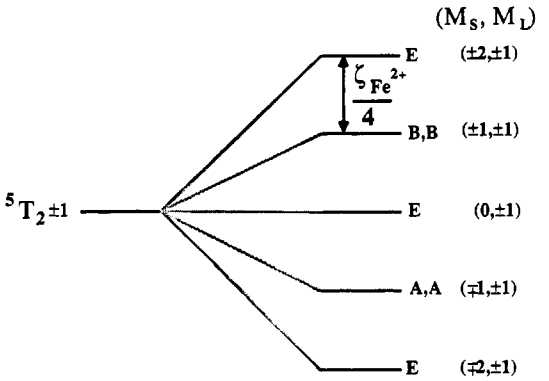

Figure 12. In-state spin–orbit splitting of the ligand-field $^5T_2(\pm1)$ state, showing the transformation properties in S_4 symmetry of the doublets. Also shown is the spin and orbital wave functions which comprise each state.

μ_B is the Bohr magneton, B is the external field, $f(E)$ is an energy-dependent band shape function, and C_0 is given[18] by eq 5.

$$C_0 = \frac{1}{|A|}\sum_{\alpha,\lambda}\langle A\alpha|L_z + S_z|J\lambda\rangle(|\langle A\alpha|m_{-1}|J\lambda\rangle|^2 - |\langle A\alpha|m_{+1}|J\lambda\rangle|^2) \quad (5)$$

α and λ are components of the irreducible representations A (ground state) and J (excited state), $|A|$ is the total degeneracy of the ground state ($|A| = 5$), and $\langle Aa|m_\pm 1|Jj\rangle$ is the dipole matrix element for absorption of right (+) or left (−) circularly polarized light.

For a molecule oriented with the magnetic field parallel to the z axis only transitions which have x,y polarized absorption intensity can be MCD active. Therefore, in the absence of spin–orbit coupling only transitions to the $^5T_2(\pm1)$ state can exhibit an MCD signal (i.e. a temperature-independent A term). In-state spin–orbit coupling provides a mechanism for the transition to the $^5T_2(\pm1)$ state to give rise to a temperature-dependent pseudo-A term, comprised of two temperature-dependent C terms of opposite sign, which are split in energy by the spin–orbit interaction. In addition, spin–orbit coupling will give intensity to the $^3\Gamma$ states causing them to become MCD active.

The $^5T_2(\pm1)$ state will exhibit an in-state spin–orbit splitting of the tenfold degeneracy into five equally spaced doubly degenerate states (3E, 2B, and 2A states in the S_4 point group (Figure 12)). The energy spacing between the doublets is $\lambda/6\sqrt{5}$, where λ is the multielectron spin–orbit coupling constant for a $^5T_2$ state. The in-state spin–orbit splitting, λ, is given by eq 6.

$$\lambda = \langle {}^5T_2||H_{so}||{}^5T_2\rangle = (\zeta_{Fe^{2+}})\frac{3\sqrt{5}}{2} \quad (6)$$

By using eq 5, the $^5E\theta \rightarrow {}^5T_2(\pm1)$ transition will give rise to a negative pseudo-A term (i.e. negative peak to higher energy), while the $^5E\epsilon \rightarrow {}^5T_2(\pm1)$ transition will give rise to a positive pseudo-A term. Spin–orbit coupling between the $^5T_2(0)$ and $^5T_2(\pm1)$ states also mixes x,y polarized intensity into the $^5E\theta \rightarrow {}^5T_2(0)$ and $^5E\epsilon \rightarrow {}^5T_2(0)$ transitions causing them to become MCD active. This mechanism causes the $^5E\epsilon \rightarrow {}^5T_2(0)$ transition to exhibit a negative C term, while the $^5E\theta \rightarrow {}^5T_2(0)$ transition will exhibit a positive C term. Thus the signs of the MCD spectrum can be used to distinguish between the two possible ground states ($d_{x^2-y^2}$ or d_{z^2}) of the ferrous complex.

As seen above, spin–orbit coupling causes the $^5E(\epsilon$ or $\theta) \rightarrow {}^3\Gamma$ transitions to gain intensity and thereby become MCD active. By using the above intensity gaining mechanism (eqs 3 and 5) MCD

(16) Briat, B.; Canit, J. C. *Mol. Phys.* **1983**, *48*, 33.
(17) Stephens, P. J. *Adv. Chem. Phys.* **1976**, *35*, 197.
(18) Piepho, S. B.; Schatz, P. N. *Group Theory in Spectroscopy*; Wiley-Interscience: New York, 1983.

selection rules have been derived assuming either a $^5E\epsilon$ or $^5E\theta$ ground state (only $M_s = \pm 2$ populated) and these are given in Table III. The sign of the MCD depends on the ground state ($^5E\epsilon$ or $^5E\theta$) for transitions to the $^3T_1(0)$, $^3T_2(0)$, $^3A_1$, and $^3A_2$ states. This also allows the two possible ground states ($d_{x^2-y^2}$ or d_{z^2}) to be distinguished.

As with the $^5T_2(\pm 1)$ states, the $^3T_1$ or $_2(\pm 1)$ states will be split by spin–orbit coupling. This splitting will cause transitions to these states to exhibit pseudo-A term MCD behavior; however, from the MCD saturation at 4 K only the $M_s = \pm 2$ sublevels are populated at low temperature ($T \approx 4$ K). In this situation the $^5E(\epsilon$ or $\theta) \rightarrow {}^3T_1(\pm 1)$ or $^5E(\epsilon$ or $\theta) \rightarrow {}^3T_2(\pm 1)$ transitions will have no x,y polarized absorption intensity (Table III). Therefore these transitions will not be MCD active and are not present in the low-temperature MCD spectrum.

(C) Band Assignments. It is clear from the x,y polarization of the absorption spectrum (Figure 5) that the state at 4600 cm^{-1}, which has an intensity (ϵ = 270 M^{-1} cm^{-1}) characteristic[8] of a spin-allowed $^5E \rightarrow {}^5T_2$ ligand-field transition, is either the $^5E\theta \rightarrow {}^5T_2(\pm 1)$ or $^5E\epsilon \rightarrow {}^5T_2(\pm 1)$ transition. On the basis of the polarized absorption of this 4600-cm^{-1} feature it is not possible to distinguish between the two ground-state possibilities. There is no evidence for a z-polarized transition, which argues for a $^5E\epsilon$ ground state, although the complex could have a $^5E\theta$ ground state with a S_4 distortion which causes the $^5E\theta(d_{z^2}) \rightarrow {}^5T_2(0)$ transition to be below 4000 cm^{-1} and thus out of the range of our spectrometer. However, on the basis of the positive sign of the pseudo-A term arising from this transition (Figure 6) the complex must have a $^5E\epsilon$ ground state. The assignment of the transition is included in Table II. As shown below, this ground state is also required by the sign of the C term arising from the lowest energy spin-forbidden transition (band C, Table I). And as shown below the observed S_4 energy splitting of the $^3T_1{}^{(b)}$ and $^3T_2{}^{(a)}$ states reveals that the d_{z^2} orbital must be 1400 cm^{-1} above the $d_{x^2-y^2}$ orbital. As this clearly defines the ground state of the $Fe(SR)_4^{2-}$ complex as the $^5E\epsilon$ state, the subsequent analysis is carried out with use of this ground state.

Bands A and B in Figure 7 are purely z polarized at 5 K and thus exhibit no low-temperature MCD signal. This is consistent with an assignment of bands A and B as the $^5E\epsilon \rightarrow {}^3T_1{}^{(a)}(\pm 1)$ and $^5E\epsilon \rightarrow {}^3T_2{}^{(a)}(\pm 1)$ transitions, respectively. These two states can be distinguished by their band widths, because the $^5E\epsilon \rightarrow {}^3T_1{}^{(a)}(\pm 1)$ transition is ligand-field dependent and should be broad, while the $^5E\epsilon \rightarrow {}^3T_2{}^{(a)}(\pm 1)$ transition is ligand-field independent and should be sharp. Band C is purely x,y polarized and exhibits a positive MCD signal (Figure 8). This is only consistent with an assignment as the $^5E\epsilon \rightarrow {}^3T_1{}^{(a)}(0)$ transition. The band width is similar to band A, supporting the assignment of band A as the other orbital component of the $^3T_1{}^{(a)}$. Bands D and E are purely x,y polarized and sharp, and they exhibit a negative MCD signal and thus must be the $^5E\epsilon \rightarrow {}^3E$ and the $^5E\epsilon \rightarrow {}^3T_2{}^{(a)}(0)$, respectively. These two states cannot be distinguished on the basis of ligand-field theory which predicts the average energy of the $^3T_2{}^{(a)}$ state to be below that of the ^3E state; however, it should be noted that because these two states are so close in energy a reversal of their assignment will have negligible effect on the ligand-field analysis presented in section D. Band E has roughly the same band width as band B, supporting the assignment of band B as the other orbital component of the $^3T_2{}^{(a)}$. Band F is purely x,y polarized and has a positive MCD and must be the $^3T_1{}^{(a)}(0)$ state. Band G is purely z polarized and must be the $^3T_1{}^{(b)}(\pm 1)$ state. Band H is dominantly x,y polarized and gives rise to a negative MCD, and therefore it could be either a $^3T_2(0)$ or $^3A_2$ state; however, ligand-field theory[19] (Figure 3) allows the $^3T_2(0)$ state to be ruled out because the $^3A_2$ state is predicted to be energetically below the $^3T_2{}^{(b)}$ state. Band I exhibits mixed polarizations and gives rise to a positive MCD. This is consistent with an assignment as both components of the $^3T_1{}^{(c)}$ state. Band J shows mixed polarizations and gives rise to a negative MCD signal. This state must contain both components of the $^3T_2{}^{(b)}$ state. These assignments are summarized in Table I and included in Figure 13a (bottom).

(D) Ligand-Field Analysis. By using the observed and assigned spin-allowed and spin-forbidden d → d transitions (Tables I and III) and the Tanabe–Sugano matrices,[19] a ligand-field analysis has been performed to extract the one-electron Fe(II) d orbital splitting pattern and to estimate the electron-repulsion parameters (B and C). The electron-repulsion parameters were adjusted to fit the energies of the ^3E and $^3A_2$ states, while the value for Dq was determined from the energy of the $^3T_2{}^{(a)}$ state. After adjusting Dq the values of B and C were readjusted, and this procedure was repeated until self-consistent values were obtained. This gives a best fit with the ligand-field parameters: C = 2800 cm^{-1}, B = 620 cm^{-1}, and Dq = −350 cm^{-1}. Calculated values for all the transitions including the S_4 energy splittings as determined below are given in Table I.

The S_4 axial splitting of the Fe 3d t_2 orbitals (d_{xy}, d_{xz}, d_{yz}) can be directly determined from the splitting in the $^3T_1{}^{(a)}$ state (Figure 3), as given by eq 7. $\Delta(^3T_1{}^{(a)})$ is the energy of the $^3T_1(\pm 1)$ state

$$\Delta(^3T_1{}^{(a)}) = -\delta \tag{7}$$

minus the energy of the $^3T_1(0)$ state, and δ is the energy of the $d_{xz,yz}$ orbitals minus the energy of the d_{xy} orbitals. As the band A, band C splitting (Figure 13) is −700 cm^{-1} the $d_{xy,yz}$ to d_{xy} splittings is 700 cm^{-1}. Therefore the $^5T_2(0)$ state should be 700 cm^{-1} below the $^5T_2(\pm 1)$ state, placing the average energy of the $^5T_2$ state at 4370 cm^{-1}. This value is higher than the $10Dq$ value of 3500 cm^{-1} as determined from the ligand-field fit to the spin-forbidden transitions. The fact that the $^5T_2$ state occurs at higher energy than $10Dq$ is mostly due to the S_4 splitting of the $^5E\epsilon$ and $^5E\theta$ states and indicates a $d_{x^2-y^2}$ to d_{z^2} splitting of 1740 cm^{-1}. This splitting can be directly estimated from the S_4 splitting of the $^3T_1{}^{(b)}$ or $^3T_2{}^{(a)}$ states (Figure 13, bottom) as expressed in eq 8, where $\Delta(^3T_1{}^{(b)}0$ and $\Delta(^3T_2{}^{(a)})$ are the energy of the doubly

$$\Delta(^3T_1{}^{(b)}) = -(3/4)\mu \tag{8a}$$

$$\Delta(^3T_2{}^{(a)}) = (3/4)\mu \tag{8b}$$

degenerate state minus the energy of the nondegenerate state and μ is the energy of the $d_{x^2-y^2}$ orbital minus the energy of the d_{z^2} orbital (Figure 14). Both of these transitions yield a splitting of 1400 cm^{-1} between the d_{z^2} and $d_{x^2-y^2}$ orbitals. Figure 14 (right side) summarizes the experimentally observed Fe(II) 3d splitting pattern.

(E) Origin of the Ground-State Zero-Field Splitting. It is generally assumed the zero-field splitting of the ^5E ground state arises from second-order spin–orbit coupling with ligand-field excited states.[5r] In T_d symmetry the ^5E state can spin–orbit couple to $^5T_2$, $^5T_1$, $^3T_2$, and $^3T_1$ states. The only $^5T_1$ states available for spin–orbit coupling are charge-transfer states which are at high energy relative to the d → d states and will have a negligible contribution to the zero-field splitting. The $^3T_2$ and $^3T_1$ states lie above 13 500 cm^{-1} (Figure 13a, Table I), so the dominant contribution to the ZFS results from the low-lying (≈4000 cm^{-1}) $^5T_2$ state. When the axial splitting of the ^5E state is large, then the contribution of the $^5T_2$ state to the spin Hamiltonian parameter, D, for a $^5E\epsilon$ ground state is given by eq 9a

$$D = -\left(\frac{\zeta^2_{Fe^{2+}}}{16}\right)\left[\frac{4}{E(^5T_2(z))} - \frac{1}{E(^5T_2(x,y))}\right] \tag{9a}$$

while for a $^5E\theta$ ground state (i.e ferrous rubredoxin)

$$D = \left(\frac{\zeta^2_{Fe^{2+}}}{16}\right)\left[\frac{4}{E(^5T_2(z))} - \frac{1}{E(^5T_2(x,y))}\right] \tag{9b}$$

where $\zeta^2_{Fe^{2+}}$ is the Fe(II) spin–orbit coupling constant. $E(^5T_2(z))$ and $E(^5T_2(x,y))$ are the energies of the S_4 axial components of the $^5T_2$ state. Note that a d_{z^2} ground state is expected to give a positive D while a $d_{x^2-y^2}$ ground state is expected to give a negative

(19) Sugano, S.; Tanbe, Y.; Kamimura, H. *Multiplets of Transition-Metal Ions in Crystals*; Academic Press: New York, 1970.
(20) Biernacki, S. W. *Phys. Stat. Sol. (b)* **1980**, *102*, 235.

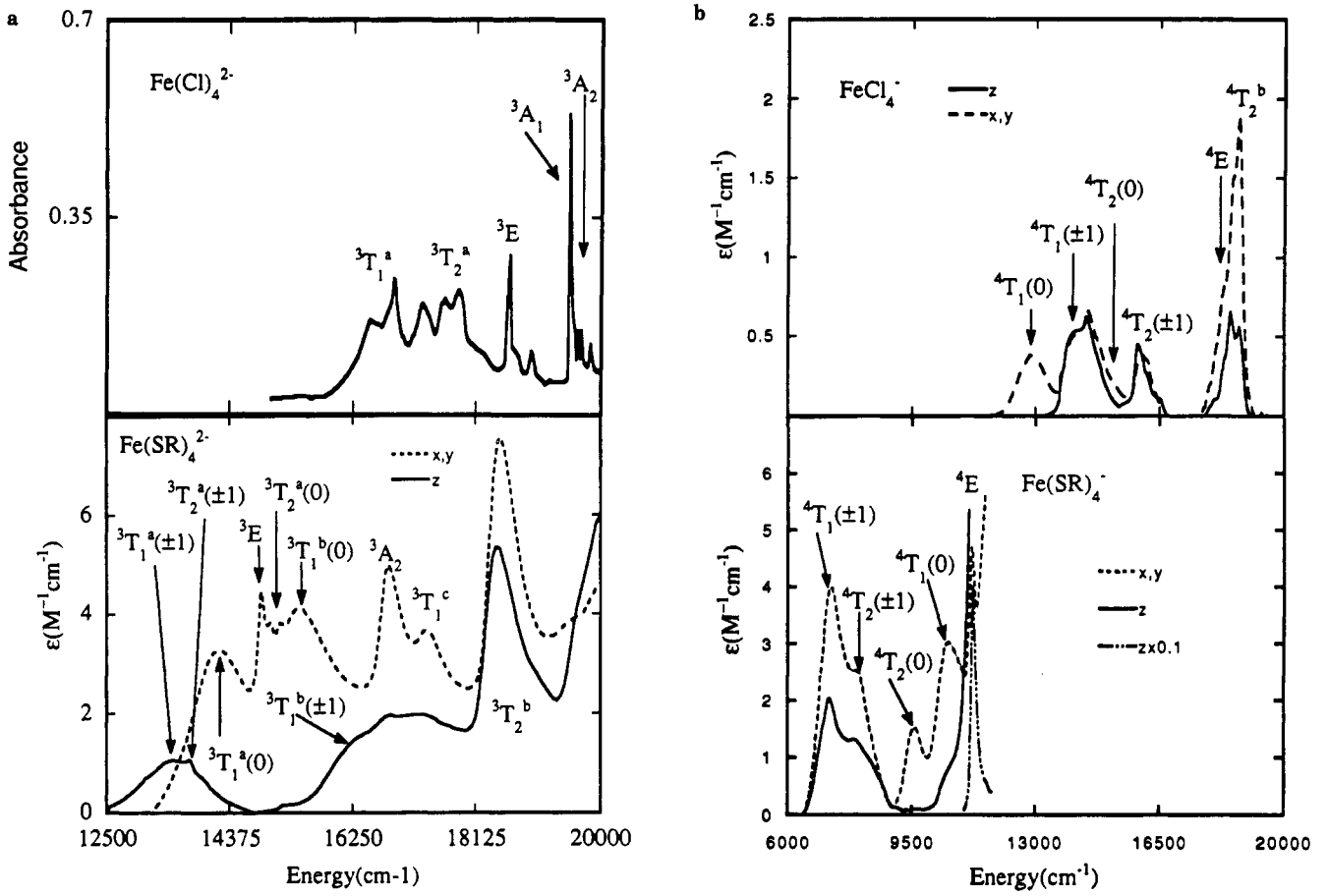

Figure 13. (a) (Top) 5 K single-crystal absorption spectrum of $FeCl_4^{2-}$ in Cs_3FeCl_5 along with band assignments as given in ref 16. (Bottom) Polarized absorption spectrum at 7 K for a 1.5 mm thick $[N(Et)_4]_2[Fe(SR)_4]$ crystal taken on the 010 face along with band assignments. (b) (Top) 5 K polarized absorption of $FeCl_4^-$ in $[P(Ph)_4][FeCl_4]$ along with band assignments as given in ref 22. (Bottom) 5 K polarized absorption of $Fe(SR)_4^-$ in $[N(Et)_4][Fe(SR)_4]$ along with band assignments as given in ref 6.

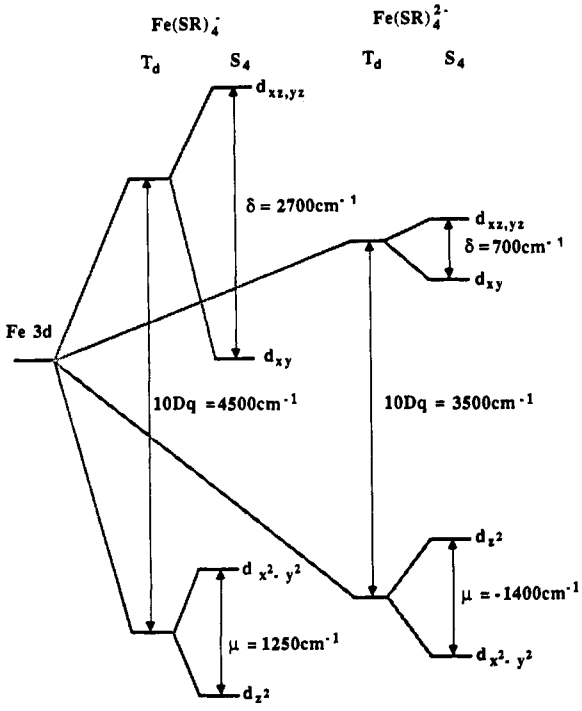

Figure 14. Fe 3d orbital splitting pattern for $Fe(SR)_4^-$ (left) as given in ref 6 and for $Fe(SR)_4^{2-}$ (right) as determined from this study.

D. By using the observed excited state energies (Table II) and the free ion spin–orbit coupling constant[20] ($\zeta_{Fe^{2+}}$ = 400 cm^{-1}), D_{calc} = −8.52 cm^{-1} whereas D_{exp} = −8.7 ± 0.7 cm^{-1}.

The $^3T_1$ and $^3T_2$ ligand-field states have the following contribution (eq 10) to the ground-state zero-field splitting, where

$$D(^3T_1) = \sum_i \frac{|\langle ^3T_{1_i}||H_{so}||^5E\rangle|^2}{120E(^3T_{1_i}(x,y))} \quad (10a)$$

$$D(^3T_2) = \sum_i \frac{|\langle ^3T_{2_i}||H_{so}||^5E\rangle|^2}{360}\left[\frac{4}{E(^3T_{2_i}(z))} - \frac{1}{E(^3T_{2_i}(x,y))}\right] \quad (10b)$$

$\langle ^3T_2||H_{so}||^5E\rangle$ and $\langle ^3T_1||H_{so}||^5E\rangle$ are reduced spin–orbit coupling matrix elements, and the sum is over all the $^3T_2$ and $^3T_1$ ligand-field states. On the basis of the observed and calculated energies for the $^3T_1$ and $^3T_2$ states, the tabulated values for the spin–orbit matrix elements, and the free ion spin–orbit coupling constant, $D_{calc}(^3\Gamma)$ = −1.5 cm^{-1}. The net triplet contribution is the same sign as the $^5T_2$ contribution thus adding 20% to the magnitude of *D*. As expected this contribution is substantially less than the $^5T_2$ contribution, but is not so small that it can be entirely neglected.

The total D_{calc} = −10 cm^{-1}; however, this ignores the covalent reduction of the free ion spin–orbit coupling constant.[21] Inclusion of an isotropic covalent reduction of the spin–orbit coupling constant to 350 cm^{-1} leads to excellent agreement with the experimental value and a reasonable reduction of 87% due to covalency. The agreement with experiment supports the earlier work of Bertrand and Gayda,[5r] relating the ZFS to ligand-field parameters of the ferrous site. The use of an isotropic reduction factor (i.e. $\kappa_{x,y} = \kappa_z$) is in contrast to the ferric systems where the

(21) Stevens, K. W. H. *Proc. R. Soc. London* **1953**, *A219*, 542.

experimental data require the inclusion of significant anisotropic covalency effects to account for the observed zero-field splitting.

Discussion

One of the most striking features to come from our spectroscopic studies of the ferric chloride[22] and ferric thiolate[6] complexes is the large shift in energy of the spin-forbidden ligand-field transitions (Figure 13b). In terms of spin-restricted ligand-field theory the reduction in energy of the ligand-field transitions from their free ion values is typically attributed to a covalent reduction of electron repulsion.[23] However, the observed lower energy shift of 7000–8000 cm^{-1} is much too large to be accounted for on the basis of reduction of electron repulsion. An alternative explanation for this energy shift has come out of spin-unrestricted self-consistent-field Xα-SW calculations on these high-spin ferric complexes. In this spin-polarized bonding model the spin-up (majority spin) and spin-down (minority spin) orbitals are not required to have the same orbital wave functions, and thus they can have different spatial distributions. In high-spin ferric complexes large-spin polarization effects have a dramatic effect on the bonding interactions, causing the complex to have an inverted bonding scheme with highest occupied spin-up orbitals localized on the ligand while the empty spin-down orbitals are localized on the metal (Figure 2). Since the spin-forbidden transitions in high-spin ferric complexes are between these orbitals, these transitions will have a large amount of charge-transfer character, and thus their energy should be affected strongly by the valence ionization energy of the ligand. As is predicted from the Xα-SW calculations, the energy of these ($^6A_1 \rightarrow {}^4\Gamma$) transitions is experimentally observed to shift by roughly the difference in valence ionization energy[7] ($\approx$1 eV) between the thiolate and chloride ligands. This inverted bonding description for the spin-up levels is also supported by valence band photoelectron spectroscopy[7] which shows that the highest occupied orbitals in $Fe(L)_4^-$ complexes have more ligand than metal character.

In contrast to the ferric $^6A_1 \rightarrow {}^4\Gamma$ transitions, the ferrous $^5E \rightarrow {}^3\Gamma$ transitions shift by $\sim$3000 cm^{-1} between the ferrous thiolate and chloride complexes[15] (Figure 13a), indicating a more traditional (normal) bonding description for the ferrous complexes, in which the highest occupied spin-up and spin-down orbitals are localized predominantly on the metal. It should be noted that none of the observed $^5E \rightarrow {}^3\Gamma$ transitions are completely independent of 10*Dq*, which accounts for some of the energy reduction. Similar energy shifts[24] have been observed in the spin-forbidden ligand-field-independent transitions for Cr^{3+} and Mn^{2+} chloride and sulfide complexes. This effect can be seen from a quantitative comparison of the electron-repulsion parameters obtained from a ligand-field fit of the $Fe(L)_4^{2-}$ $^5E\epsilon \rightarrow {}^3\Gamma$ and $Fe(L)_4^-$ $^6A_1 \rightarrow {}^4\Gamma$ transition energies (L = Cl^- or SR^-). This analysis yields B = 620 cm^{-1} and C = 2800 cm^{-1} for the ferrous tetrathiolate, which are similar to values obtained for a FeS_4^{2-} complex[25] and represent a reasonable reduction ($\approx$70%) of electron repulsion due to covalency ($B_{\text{free ion}}$ = 950 cm^{-1}, $C_{\text{free ion}}$ = 3652 cm^{-1}).[26] In the $Fe(CL)_4^{2-}$ complex B = 830 cm^{-1} and C = 3430 cm^{-1}. B and C are reduced by 80% for the thiolate relative to the chloride complex, indicating a more covalent bonding interaction.[23] In contrast to the ferrous complexes, the ferric complexes exhibit an extreme reduction in B and C (B = 22 cm^{-1} and C = 2222 cm^{-1} in the $Fe(SR)_4^-$ complex[6] versus B = 444 cm^{-1} and C = 2728 cm^{-1} in the $Fe(Cl)_4^-$ complex,[22] where electron repulsion is already reduced by 55% from the free ion values). The reduction in B (to 5% of the chloride value) is so large that the electron-repulsion parameters obtained are meaningless.

The fact that the bonding scheme (Figure 2) found for the Fe^{3+} complexes is inverted while the Fe^{2+} complexes have a more normal bonding scheme indicates that a large electronic relaxation

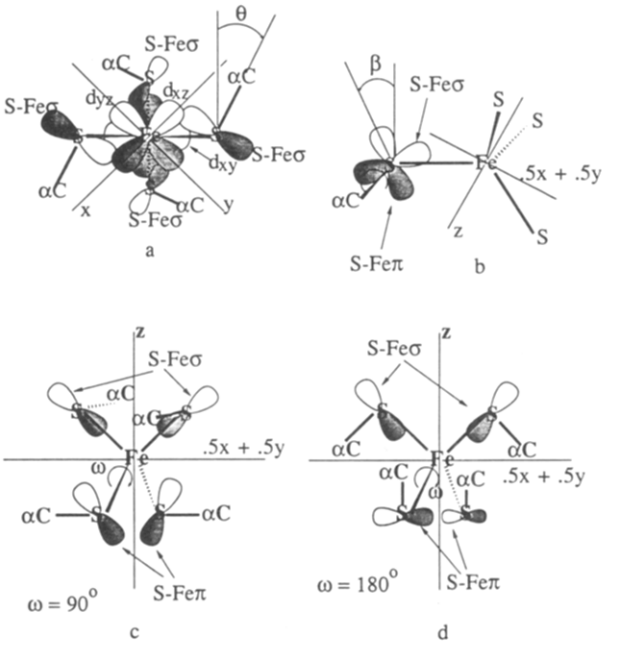

Figure 15. (a) View down the molecular z axis showing the effect of the αC bond angle (>90°) on the orientation of the S–Feσ orbital relative to the Fe $d_{xz,yz}$ and d_{xy} orbitals. (b) View down one of the αC–S bonds showing the effect of the rotation (β) on the orientations of the S–Feσ and S–Feπ orbitals relative to the iron center. (c) View perpendicular to the molecular z axis showing the orientations of the S–Feσ and S–Feπ orbitals relative to the iron center when ω = 90°. (d) View perpendicular to the molecular z axis showing the orientations of the S–Feσ and S–Feπ orbitals relative to the iron center when ω = 180°.

effect must take place upon reduction of the Fe^{3+}. The majority of the relaxation will take place in the spin-up orbitals which must go from being mostly ligand centered in the ferric complex to mostly metal centered in the ferrous complex. This difference in bonding results form the lower Fe 3d valence ionization energy and reduced exchange splitting for the Fe(II) complex relative to the Fe(III).

Figure 14 compares the experimentally observed $Fe(SR)_4^{2-}$ 3d orbital splitting pattern with our previously observed pattern for the $Fe(SR)_4^-$ complex.[6] Both of these complexes have a similar D_{2d} compression of the $Fe(S)_4$ core along the molecular S_4 axis (114.4° in the Fe(III) complex versus 113.4° in the Fe(II) complex).[27] The only significant geometric difference between the $Fe^{II}(S)_4$ and $Fe^{III}(S)_4$ cores is the 0.04 Å increase in the Fe–S bond lengths in the Fe(II) complex. While these two complexes have minor structural differences in the $Fe(S)_4$ core there are clear quantitative and qualitative differences (Figure 14) in the 3d bonding interactions in these complexes. On going from Fe(III) to Fe(II) a reduction is seen in the magnitude of δ (Figure 14). This can be reasonably accounted for on the basis of the larger energy separation between the Fe(II) 3d levels and thiolate valence levels, which is evidenced by the lack of visible charge-transfer transitions in the Fe(II) complex and is due to the lower valence ionization energy of the Fe(II) 3d levels. While the sign of δ is the same, μ changes sign, which can be explained on the basis of the relative orientation of the thiolate valence orbitals which produce a negative μ for the ferrous complex and a positive μ for the ferric complex.

The dominant bonding interaction experienced by the sulfur 3p valence orbitals is with the αC, which causes one of the S 3p orbitals (S–Cσ) to be at low energy, and directed toward the αC. In the free thiolate ligand the other two sulfur 3p orbitals will be oriented perpendicular to the S–Cσ bond, and either perpendicular or parallel to the phenyl ring.[28] These two S 3p orbitals

(22) Deaton, J. C.; Gebhard, M. G.; Solomon, E. I. *Inorg. Chem.* **1989**, *28*, 877.
(23) Ferguson, J. *Prog. Inorg. Chem.* **1970**, *12*, 195.
(24) Jorgensen, C. K. *Prog. Inorg. Chem.* **1962**, *4*, 73.
(25) Skowronski, M.; Liro, Z. *J. Phys. C* **1982**, *15*, 137.
(26) Ferguson, J.; Guggenheim, H. J.; Krausz, E. R. *Aust. J. Chem.* **1969**, *22*, 1809.

(27) It is interesting to note that the D_{2d} distortion of the FeS_4 core in the ferrous complex is smaller than in the ferric complex, indicating that the geometry of these ferrous complexes is controlled more by steric effects and crystal packing forces than by a Jahn–Teller effect.

are σ and π bonding to the Fe, and the extent of the S–Feσ and S–Feπ bonding interaction is controlled by the orientation of the S–αC bond relative to the Fe–S bond.

Three rotations of the thiolate determine the interaction of the sulfur valence orbitals with the Fe(II) 3d orbitals, and thus the Fe 3d splitting. The Fe–S–αC bond angle is typically >90°. This polar coordinate, θ, is depicted in Figure 15a, which shows the view down the z axis of the S_4 complex. For clarity only the S–Feσ valence orbitals have been included as the S–Feπ orbital is coming out of the plane of the page. In addition to the ligand orbitals, the Fe d_{xy} orbital and two lobes for both the d_{xz} and d_{yz} orbitals are shown in this view. As shown in the figure this rotation ($\theta \approx 10$–20°) causes the S–Feσ bonding orbital to be rotated off the Fe–S bond, while leaving it in the Fe–S–αC plane. The S 3pπ orbital remains unchanged by this rotation. The second rotation,[29] β, is about the S–αC bond and is depicted in Figure 15b where two of the Fe–S bonds are in the plane of the page as are the lines depicting the angle β and the S–C bond is perpendicular to the page. In this view the molecular z axis is in the plane of the page. For clarity only one αC is shown. As with the θ rotation, the β rotation causes the S–Feσ orbital to be rotated off the Fe–S bond (Figure 15b), while leaving it in the S–Fe–S plane (i.e. the plane of the page). This rotation will mix the S–pπ and S–pσ orbitals. The third rotation, ω, is about the Fe–S bond and is determined by the dihedral angle between the S–Fe–S plane and the Fe–S–αC plane. This rotation is depicted in Figure 15, parts c (ω = 90°) and d (ω = 180°). In this view the molecular z axis is in the plane of the page which bisects the x,z and y,z molecular planes. For clarity only two of the S–Feσ and S–Feπ orbitals are shown in each figure. This rotation will affect the S–Feπ orbital by causing it to be oriented parallel (Figure 15d, ω = 180°) to the x,y plane of the molecule thus maximizing overlap with the Fe $d_{x^2-y^2}$ orbital, or oriented in the ($0.5x \pm 0.5y$) molecular planes (Figure 15c, ω = 90°) thus maximizing overlap with the d_{z^2} orbital. When ω = 180° (Figure 15d) the θ rotation causes the S–Feσ to be rotated toward the x,y plane of the complex therefore increasing the antibonding interaction with the Fe d_{xy} and $d_{x^2-y^2}$ orbitals. When ω = 90° (Figure 15c) the θ rotation causes the S–Feσ to be rotated off the d_{xy} orbital (Figure 15a) thus decreasing the S–Feσ overlap with the d_{xy} orbital while leaving overlap with the $d_{xz,yz}$ unchanged. In this orientation the θ rotation will cause the S–Feσ orbital to have nonzero overlap with the $d_{x^2-y^2}$ orbital, but the S–Feσ d_{z^2} overlap will remain negligible, thus causing μ to be positive. When ω = 0° the S–Feσ orbital will be rotated away from the x,y plane (i.e. the opposite of Figure 15d) decreasing overlap with the d_{xy} orbital and $d_{x^2-y^2}$ orbitals.

On the basis of the crystal structure[30] of the ferrous tetrathiolate complex (Figure 4), the phenyl ring is within −13.5° (β = −13.5°) of being parallel to the Fe–S bond meaning the S 3p orbital which is parallel to the phenyl ring is involved in σ bonding to the Fe 3d orbitals. The other S 3p orbital which is conjugated with the phenyl ring is involved in S–Feπ bonding. The Fe–S–C bond angle is 111.6° (θ = 21.6°), and the dihedral angle (ω) is 47.6°. For this dihedral angle the S–Feπ orbital will have equal overlap with the d_{z^2} and $d_{x^2-y^2}$ orbitals and equal overlap with the $d_{xz,yz}$ and d_{xy} orbitals, meaning the S–Feπ interaction cannot be responsible for the observed S_4 axial splitting. The Fe–S–αC bond angle of 111.6° rotates the S 3pσ orbital off the Fe–S bond, causing the S–Feσ orbitals to have greater overlap with $d_{xz,yz}$ orbitals destabilizing them relative to the d_{xy} orbital. In addition, the combination of the θ and β rotations will cause the S–Feσ orbital to be rotated away from the molecular x,y plane decreasing overlap with the $d_{x^2-y^2}$ orbital while significantly increasing overlap and thus destabilizing the d_{z^2} orbital (Figure 14, right).

The major structural difference between the ferrous and ferric model complexes is the angle ω which is 90° in the ferric complex. The other angles in the ferric model complex are θ = 12° and β = 2°. On the basis of these angles the S–Feσ overlap with the $d_{xz,yz}$ orbitals should be greater than the overlap with the d_{xy} orbital (Figure 15a). On the basis of the S–Feσ interaction the sign of the axial splitting (δ) will be positive as it is in the ferrous complex. In contrast to the ferrous complex, the orientation of the S–Feσ orbital in the ferric complex results in net overlap with the $d_{x^2-y^2}$ orbital; however, the d_{z^2} orbital will remain nonbonding with the S–Feσ orbital. Therefore the S–Feσ interaction causes μ to be positive in the ferric complex but negative in the ferrous complex (Figure 14).

The fact that μ changes sign between the ferric and ferrous model complexes demonstrates the strong αC orientation dependence of the Fe 3d orbital splitting. The sensitivity of the ground state to the different orientations of the αC is clearly evidenced by the fact that ferrous rubredoxin has a d_{z^2} ground state. While the magnitude of the d_{z^2} to $d_{x^2-y^2}$ splitting in ferrous rubredoxin is not known, Mossbauer data indicate it must be greater than 1000 cm^{-1}. In *Cp* rubredoxin the dihedral angle, ω, is approximately 180°, causing the S–Feσ orbital to be rotated toward the molecular x,y axis (Figure 15d) decreasing overlap with d_{z^2} while increasing overlap destabilizing $d_{x^2-y^2}$ relative to d_{z^2}. The S–Feπ orbital can only overlap with $d_{x^2-y^2}$ (Figure 15d), increasing the magnitude of μ; however, on the basis of the ferric thiolate study the S–Feπ interaction should not contribute significantly to μ. In *Cp* rubredoxin the d_{z^2} orbital should be virtually nonbonding with respect to the thiolate valence orbitals, and it is expected that the d_{z^2} to $d_{x^2-y^2}$ splitting in ferrous rubredoxin will be quite large ($|\mu| > 1000$ cm^{-1}), which could explain the rather high energy (≈6000 cm^{-1}) of one of the components of the $^5E\theta(d_{z^2}) \rightarrow {}^5T_2$ transition.

In summary, a large electronic relaxation has been found to take place upon reduction of ferric thiolate complexes, and a strong αC orientation dependence of the d_{z^2} and $d_{x^2-y^2}$ energies is observed. The dramatic relaxation which has been demonstrated to take place will make a significant contribution to electron-transfer processes by reducing the ionization energy (i.e. reduction potential) and by affecting the wave functions of the orbitals involved in the electron transfer, and thus affecting[31] the rate of electron transfer. The αC orientation dependence is significant as it provides a mechanism by which the protein can control the energy of the orbital which is donating or accepting the electron, thus lowering the transition-state energy for the electron-transfer process. In addition, the energy splitting of the d_{z^2} and $d_{x^2-y^2}$ orbitals by the S–Feσ bonding interaction will quench the Jahn–Teller distorting force which would be present in the ferrous complex if these two orbitals were degenerate.

Acknowledgment. We thank the National Science Foundation [Grant CHE-8919687 (E.I.S.)] and the National Institutes of Health [Grants GM-36308 (M.M), GM-28386 (P.J.S.), and GM-31849 (S.A.K.)]. M.S.G. acknowledges NSF for a graduate research fellowship.

Registry No. $[Et_4N]_2[Fe(SR)_4]$ (R = 2-(Ph)C_6H_4), 131437-15-5; LiSR (R = 2-(Ph)C_6H_4), 131437-13-3; $FeCl_3$, 7758-94-3; $[Et_4N]_2(Zn(SR)_4)$, 131437-17-7; $[Fe(SR)_4]^{2-}$, 131437-14-4; $[Zn(SR)_4]^{2-}$, 131437-16-6; $FeCl_4^{2-}$, 17611-27-7; $Fe(SR)_4^-$, 131437-18-8.

(28) In rubredoxin the Fe is coordinated to an alkyl thiolate sulfur as opposed to an aryl thiolate. The phenyl ring slightly perturbs the energy of the S 3p orbital which is perpendicular to the phenyl ring, but this will be a minor effect.

(29) This rotation is only important for the aryl thiolate complexes because conjugation of the S 3p orbitals into the phenyl ring will lead to a difference in the energy and character of the two S 3p orbitals, and thus the orientation of the phenyl ring will effect the bonding interactions in the complex.

(30) The phenyl ring in the 2 position is oriented perpendicular to the main phenyl ring and will not be conjugated into the thiolate ring system.

(31) Newton, M. D. *J. Phys. Chem.* **1986**, *90*, 3734.